JOURNAL OF GEOPHYSICAL RESEARCH, VOL. 103, NO. B12, PAGES 30,131–30,145, DECEMBER 10, 1998

Poroelastic rebound along the Landers 1992 earthquake surface rupture

Gilles Peltzer, Paul Rosen, and Francois Rogez

Jet Propulsion Laboratory, California Institute of Technology, Pasadena

K. Hudnut

U.S. Geological Survey, Pasadena, California

Abstract Maps of surface displacement following the 1992 Landers, California, earthquake, generated by interferometric processing of ERS-1 synthetic aperture radar (SAR) images, reveal effects of various postseismic deformation processes along the 1992 surface rupture. The large-scale pattern of the postseismic displacement field includes large lobes, mostly visible on the west side of the fault, comparable in shape with the lobes observed in the coseismic displacement field. This pattern and the steep displacement gradient observed near the Emerson-Camp Rock fault cannot be simply explained by afterslip on deep sections of the 1992 rupture. Models show that horizontal slip occurring on a buried dislocation in a Poisson's material produces a characteristic quadripole pattern in the surface displacement field with several centimeters of vertical motion at distances of 10-20 km from the fault, yet this pattern is not observed in the postseismic interferograms. As previously proposed to explain local strain in the fault step overs [*Peltzer et al.*, 1996b], we argue that poroelastic rebound caused by pore fluid flow may also occur over greater distances from the fault, compensating the vertical ground shift produced by fault afterslip. Such a rebound is explained by the gradual change of the crustal rocks' Poisson's ratio value from undrained (coseismic) to drained (postseismic) conditions as pore pressure gradients produced by the earthquake dissipate. Using the Poisson's ratio values of 0.27 and 0.31 for the drained and undrained crustal rocks, respectively, elastic dislocation models show that the combined contributions of afterslip on deep sections of the fault and poroelastic rebound can account for the range change observed in the SAR data and the horizontal displacement measured at Global Positioning System (GPS) sites along a 60-km-long transect across the Emerson fault [*Savage and Svarc*, 1997]. Using a detailed surface slip distribution on the Homestead Valley, Kickapoo, and Johnson Valley faults, we modeled the poroelastic rebound in the Homestead Valley pull apart. A Poisson's ratio value of 0.35 for the undrained gouge rocks in the fault zone is required to account for the observed surface uplift in the 3.5 years following the earthquake. This large value implies a seismic velocity ratio V_p/V_s of 2.1, consistent with the observed low V_s values of fault zone guided waves at shallow depth [*Li et al.*, 1997]. The SAR data also reveal postseismic creep along shallow patches of the Eureka Peak and Burnt Mountain faults with a characteristic decay time of 0.8 years. Coseismic, dilatant hardening (locking process) followed by post-seismic, pore pressure controlled fault creep provide a plausible mechanism to account for the decay time of the observed slip rate along this section of the fault.

1. Introduction

The M_w=7.3, Landers earthquake of June 28, 1992, produced a 75-km-long surface rupture with ~3 m average and up to 6.2 m of right-lateral displacement (Figure 1) [*Hart et al.*, 1993; *Sieh et al.*, 1993]. In the months and years following the earthquake, postseismic surface displacement has been monitored by repeated surveys of Global Positioning System (GPS) networks, trilateration arrays, and creep meters. Fault slip models based on the GPS data in the first year after the earthquake indicate that postseismic displacement of <10 cm occurred along the northern and central sections of the fault and of up to 18 cm along the southern Johnson Valley and Eureka Peak faults [*Shen et al.*, 1994]. This amount of afterslip accounts for a postseismic strain release equivalent to 15% of the coseismic moment and is associated with a decay time of 34 days [*Shen et al.*, 1994]. Data recorded by remote (65-100 km) stations of the Southern California Permanent GPS Geodetic array (PGGA) also show postseismic displacement of up to 15% of the coseismic signal [*Bock et al.*, 1997; *Wdonwinki et al.*, 1997]. Postseismic displacements of the nearest sites indicate a decay time of 22±10 days, consistent with the previous estimate made by *Shen et al.* [1994], superimposed on a longer-term, interseismic trend [*Wdonwinski et al.*, 1997]. *Savage and Svarc* [1997] interpreted surface displacement data from a linear GPS array across the Emerson fault in the 3.4 years after the earthquake as resulting from up to 1 m of right-lateral slip on the section of the fault below a depth of 10 km. The temporal behavior of

Paper number 98JB02302.
0148-0227/98/98JB-02302$09.00

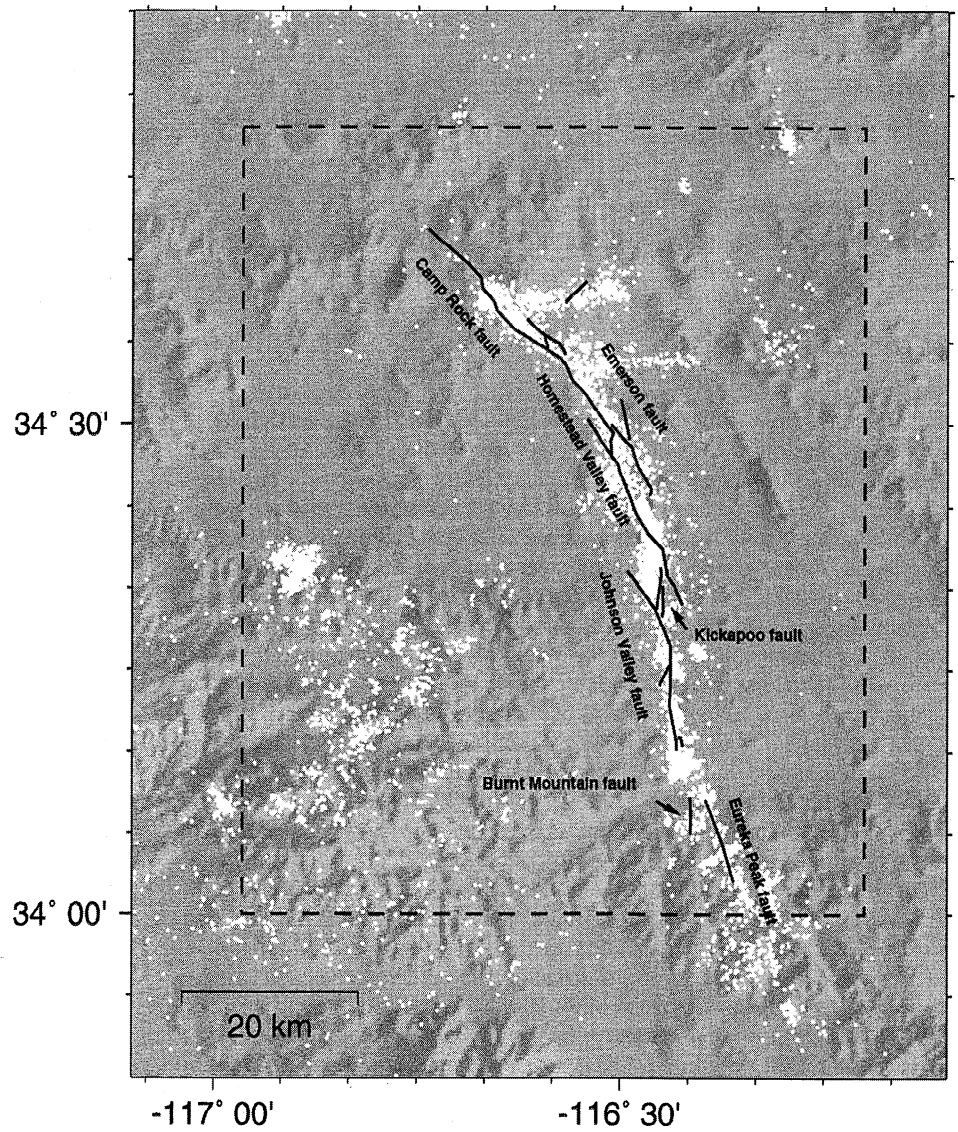

Figure 1. Map of the June 28, 1992, Landers earthquake area. Solid line is earthquake surface rupture [*Sieh et al.*, 1993]. Shade depicts topography from U.S. Geological Survey (USGS) digital elevation model. White dots are aftershocks between August 7, 1992, and January 23, 1996 [*Hauksson et al.*, 1993]. Box indicates area covered by SAR data shown in Plate 1.

their data is described by a short-term (84±23 days) exponential relaxation superimposed on an apparently linear trend. Surveys of small-aperture trilateration arrays revealed minor horizontal displacement across the 1992 surface rupture in the 5 months following the earthquake. Virtually no displacement was recorded along the Emerson Camp-Rock fault, ~9 mm along the Johnson Valley fault and up to 40 mm along the Eureka Peak fault [*Sylvester*, 1993]. Creep meters installed on the Eureka Peak fault after the earthquake have recorded up to 23 cm of surface slip in 1 year [*Behr et al.*, 1994].

However, except the continuous GPS measurements at remote stations of the PGGA, all instruments listed above provide no or poor estimates of the vertical displacement of the ground. Furthermore, point-positioning geodetic techniques are limited by the spatial range they are able to sample given the number and spacing of geodetic monuments they use. In this paper we take a new look at postseismic processes using surface displacement maps of the Landers 1992 earthquake area generated by synthetic aperture radar (SAR) interferometry (InSAR). The advantages and complementary character of InSAR are to provide a quasi-continuous map view of the displacement field over broad areas, allowing us to detect and analyze surface displacement patterns of various spatial scales, and to have great sensitivity to vertical ground displacement. The largest postseismic ground displacements and displacement gradients observed in the radar maps lie within 10 km of the 1992 surface break, at a scale that is both too short to be observed using the existing GPS arrays and too long to be observed in the near-field trilateration and creep meter data. In section 2 we briefly describe the approach and the data analysis strategy for the detection of slow deformation processes. In the following sections we discuss successively (1) afterslip and poroelastic

rebound along the Emerson-Camp Rock fault, (2) poroelastic rebound in the Homestead Valley pull-apart structure, and (3) surface creep along the southern sections of the 1992 break.

2. Approach

The phase of each pixel of a SAR complex image provides a measure (modulo half the radar wavelength) of the path length between the antenna and the ground. The technique of SAR interferometry consists of combining two SAR complex images of a given area to form an interferogram [*Gabriel et al.*, 1989]. The phase of each pixel in the interferogram is the difference between the phase of the corresponding pixels in each of the two original images. Its variation throughout the scene depicts the variation of the antenna-ground path length difference between the two images. If the images are acquired from slightly different locations, the interferometric phase is sensitive to the topography within the scene because of the small parallax between the two lines of sight [*Zebker et al.*, 1994a; *Rosen et al.*, 1995]. If the images are acquired at different times, the interferometric phase is also sensitive to any displacement of the ground along the radar line of sight that occurred during the time interval spanned by the image pair. The sensitivity of the phase to the topography increases with the distance separating the two antenna locations (baseline) at times of data acquisition. To generate a line of sight surface displacement map, it is necessary to remove the topographic signal from the interferogram. This can be achieved by either (1) simulating the topographic phase using a digital elevation model and with knowledge of the geometry of the interferometric system (two-pass method [e.g., *Massonnet et al.*, 1993; *Murakami et al.*, 1996]) or (2) generating two interferograms out of three or four SAR images of the same area and computing the phase difference of the two to eliminate the topographic phase signal common to both interferograms (three- or four-pass method [e.g., *Gabriel et al.*, 1989; *Zebker et al.*, 1994b; *Peltzer and Rosen*, 1995]). This method requires one phase field to be unwrapped and scaled to the same sensitivity to topography as the other phase field by the ratio of their baselines. In the absence of additional signal such as that produced by variations of the phase propagation delay in the wet troposphere [*Massonnet and Feigl*, 1995; *Goldstein*, 1996; *Zebker et al.*, 1997], the remainder is a map of the component of the surface displacement field parallel to the radar line of sight.

To measure surface deformation related to the slow, postseismic deformation processes after the 1992 Landers earthquake with ERS SAR data, we selected pairs of images spanning long time intervals in order to integrate surface deformation over sufficient time to be detectable by the radar. We also chose pairs having a small spatial baseline to minimize the sensitivity to topography and removed the topographic phase using one of the methods mentioned above depending on orbit configuration. For image pairs with spatial baselines smaller than 20 m, we found the U.S. Geological Survey (USGS) 90-m digital elevation model accuracy of 30 m acceptable to remove the topographic phase using the two-pass approach. In fact, for the ERS C band radar (wavelength of 56 mm), an elevation error of 30 m in the topographic map would produce a phase shift of 0.3 rad in a 20-m baseline interferogram, corresponding to an error of 2 mm in the range displacement map.

3. Analysis of Near-Field, Postseismic Deformation

We analyzed SAR data acquired from ERS tracks 399 and 127, which both cover the Landers earthquake area. The time intervals spanned by the data are shown in Figure 2. The images cover the Eastern Mojave Shear Zone, formed of several NW-SE, strike-slip faults, including the Emerson-Camp Rock and the Johnson Valley faults that ruptured during the 1992 earthquake. Geologic and geodetic data indicate that the shear zone accommodates ~15% of the Pacific-North America plate motion [*Dokka and Travis*, 1990; *Savage et al.*, 1990; *Sauber et al.*, 1994]. If ~10 mm/yr of right-lateral shear are distributed across the 100-km-wide, NW-SE shear zone, such a rate would project into a line of sight displacement rate of 3.2 mm/yr. In 3 years, this change rate would imply 9.6 mm (1/3 of a phase cycle) of line of sight displacement, distributed across the 100-km-wide SAR swath. Although it should be taken into account by proper modeling in the analysis of the far-field postseismic displacements, the small amplitude of the long-term signal and the width over which it is distributed suggest that such a correction is not required for the near- and intermediate-field displacement analysis presented here.

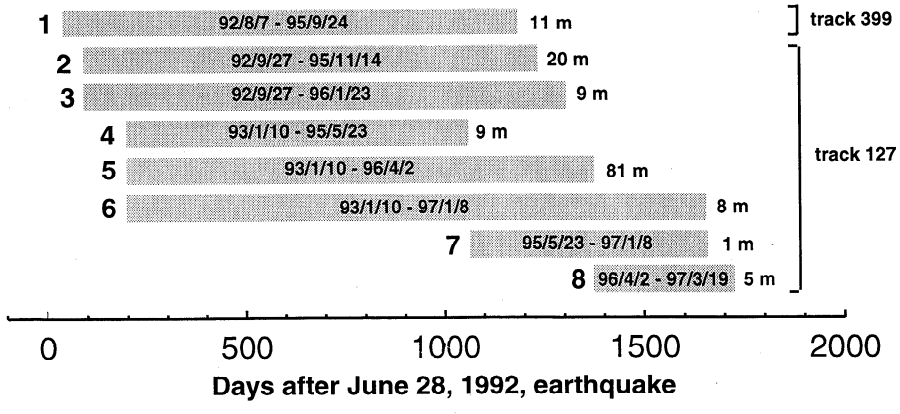

Figure 2. Time intervals covered by SAR data used in this study. Numbers indicate perpendicular component of baselines (distance between orbits, perpendicular to radar line of sight) in meters at latitude 34°20'.

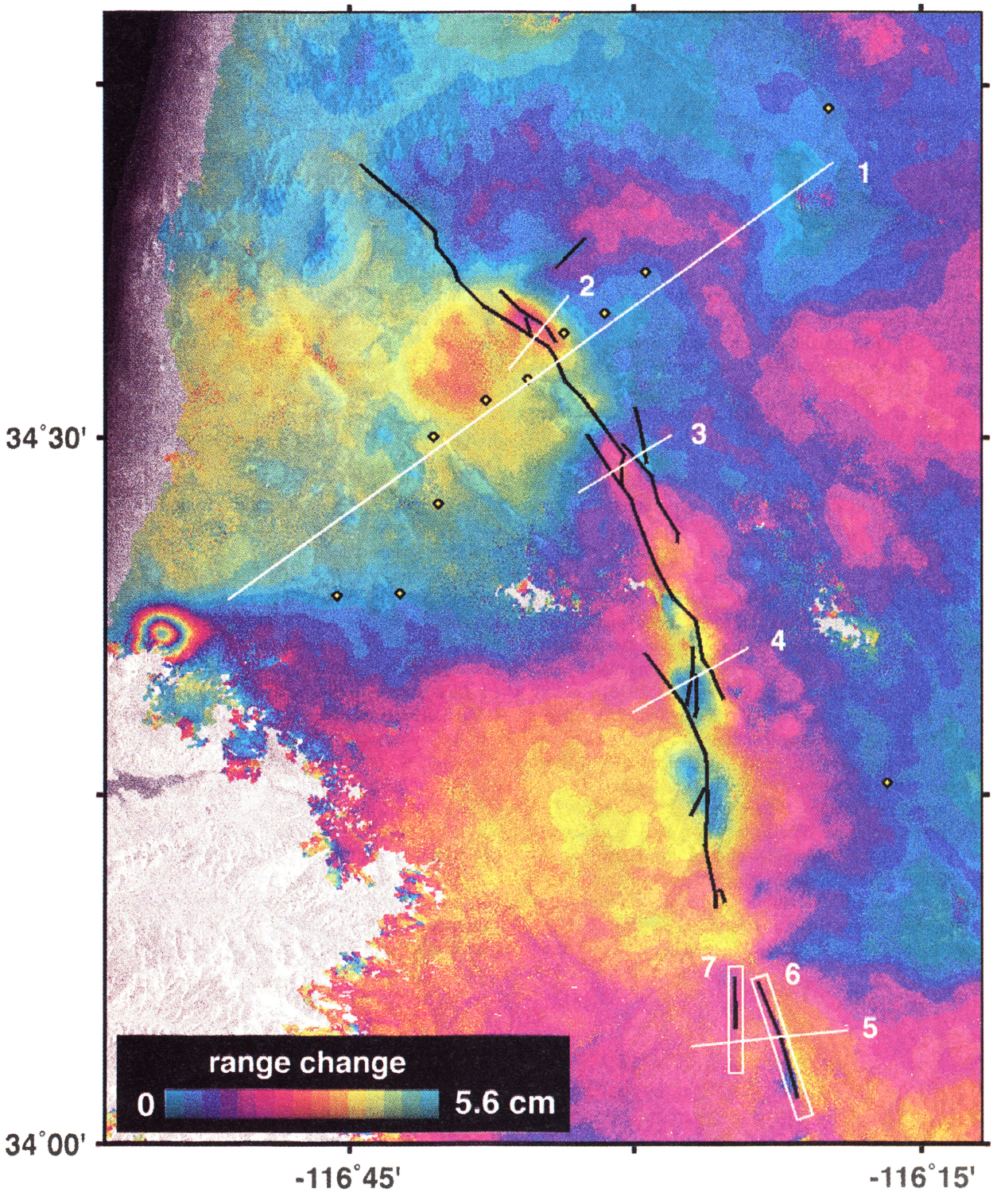

Plate 1. Interferometric map of the Landers area generated with SAR image covering the September 27, 1992, to January 23, 1996, time period. Colors overlaying backscatter radar image represent ground displacement in the direction of the satellite. Coordinates of vector pointing to ERS satellite at midswath in local east-north-up reference frame are 0.381, -0.088, 0.920 [*European Space Agency*, 1992]. Gray areas are zones where phase could not be unwrapped due to signal decorrelation between two SAR images. Black lines depict 1992 surface rupture. White lines indicate profiles shown in Figures 3, 4, 6, 8b, and 9a. Yellow diamonds show locations of GPS stations used by *Savage and Svarc* [1997]. Concentric fringes on left side of image result from $M5.4$, shallow aftershock of December 4, 1992 [*Feigl et al.*, 1995].

Plate 1 shows the interferogram covering the time interval between September 27, 1992, and January 23, 1996. Surface deformation patterns of various spatial scales are visible in the interferogram. (1) A large lobe, west of the Emerson-Camp Rock fault indicates that the ground moved away from the satellite in this area. Preliminary interpretations of this pattern suggested that it might be due to afterslip on deep sections of the fault [*Massonnet et al.*, 1996; *Peltzer et al.*, 1996a]. (2) Zones of large strain concentrated in the step overs of the 1992 rupture have been explained by postseismic rebound caused by the dissipation of pore fluid pressure gradients produced by the earthquake in the few years following the event [*Peltzer et al.*, 1996b]. (3) Sharp cuts observed in the displacement maps along the Eureka Peak and Burnt Mountain faults indicate that these faults underwent postseismic surface creep [*Behr et al.*, 1994; *Peltzer et al.*, 1996a]. In sections 3.1-3.3 we discuss in more detail these features of the postseismic displacement field and compare them with GPS data and predictions of elastic and poroelastic models.

3.1 Right-Lateral Afterslip and/or Poroelastic Rebound Along the Emerson-Camp Rock Fault

Right-lateral afterslip has been advocated to explain the surface displacement observations after the Landers 1992 earthquake made with both campaign GPS measurements [*Shen et al.*, 1994; *Savage and Svarc*, 1997] and continuous GPS measurements at remote PGGA stations [*Bock et al.*, 1997; *Wdonwinski et al.*, 1997]. *Savage and Svarc* [1997] proposed a model of afterslip based on repeated GPS measurements of a 40-km-long transect across the Emerson fault in the 3.4 years after the earthquake (Plate 1). The GPS array runs through the large, lobed pattern of deformation observed in the SAR data and crosses the 1992 rupture a few kilometers south of the compressive jog of the Emerson-Camp Rock fault where postseismic subsidence was observed during the same time period [*Peltzer et al.*, 1996b]. Figure 3 shows range change profiles for seven different time intervals (profile 1 in Plate 1) running approximately parallel to the GPS array used by *Savage and Svarc* [1997]. The discrepancies between these profiles result from the sensitivity of SAR measurements to error sources such as variations in tropospheric conditions and surface conditions. For example, the large bump observed in profiles 2 and 3 between 10 and 20 km east of the fault is a topography residual that is probably caused by an anomalous phase propagation delay in the image of September 27, 1992, common to both profiles. Because water vapor density in the lower atmosphere decreases exponentially with increasing elevation [*Gill*, 1982], changes in atmospheric conditions between the epochs of data acquisitions produce a signal that, in some instances, correlates with topography [e.g., *Delacourt et al.*, 1998]. The phase appears to be generally noisier in the 15-km-long section west of the fault than along other sections of the profiles. This region corresponds to the area where *Zebker et al.* [1994b] observed distributed surface cracks in the coseismic interferogram. Nevertheless, several features appear to be stable between these profiles and can be related with confidence to actual ground displacements in the 4 years following the Landers earthquake. All profiles clearly show that the ground moved away from the satellite west of the fault and toward the satellite east of it, a pattern that is apparently consistent with right-lateral shear parallel to the fault

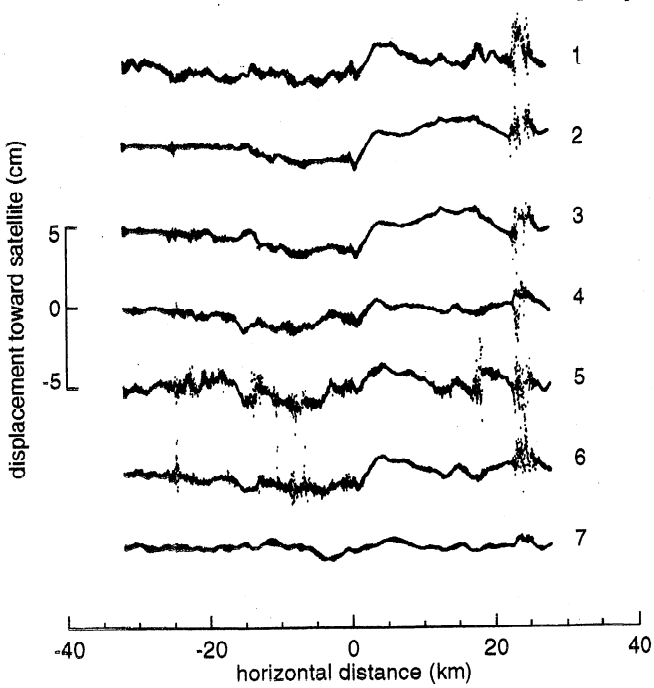

Figure 3. Line of sight surface displacement along 40-km-long, 800 m-wide profile across Emerson-Camp Rock fault (profile 1 in Plate 1) observed in seven interferometric change maps. Numbers refer to corresponding time intervals in Figure 2.

[*Massonnet et al.*, 1996, *Peltzer et al.*, 1996a]. Overall, the displacement profiles are generally symmetric with respect to a point slightly east of the 1992 surface break, with a maximum amplitude in the 4 years following the earthquake of ~5% of the coseismic signal amplitude. The profiles also show a steep displacement gradient in the 1-5 km section east of the 1992 surface break, with an amplitude that depends on both the starting date and the duration of the corresponding time interval. A decay time of 1.6±0.4 years can be derived by fitting the amplitude data to an exponentially decaying function. If these characteristics of the observed range change were due to pure, right-lateral shear parallel to the direction of the fault, the amplitude and steep gradient near the fault would require a source with its upper edge as shallow as 1.5 km and with ~0.3 m of right-lateral afterslip [*Peltzer et al.*, 1996a].

However, we argue below that the steep gradient and part of the observed range change near the fault are more likely due to vertical (and, to a lesser extent, fault-perpendicular, horizontal) motion induced by poroelastic rebound rather than due to right-lateral shear as previously inferred. Our argument is based on the general result of elastic modeling that any reasonable distribution of horizontal slip on a vertical dislocation buried in an elastic medium will produce four lobes of vertical displacement at the surface in the four quadrants determined by the fault and its perpendicular direction. In the particular case of strike-slip on a shallow fault patch, these lobes are located near the ends of the dislocation patch. Because the SAR is more sensitive to vertical ground shifts than it is to horizontal displacements, if afterslip were the only postseismic process accounting for the observed displacement field, such lobes should be prominent in the interferograms. However, they are not observed in the SAR data.

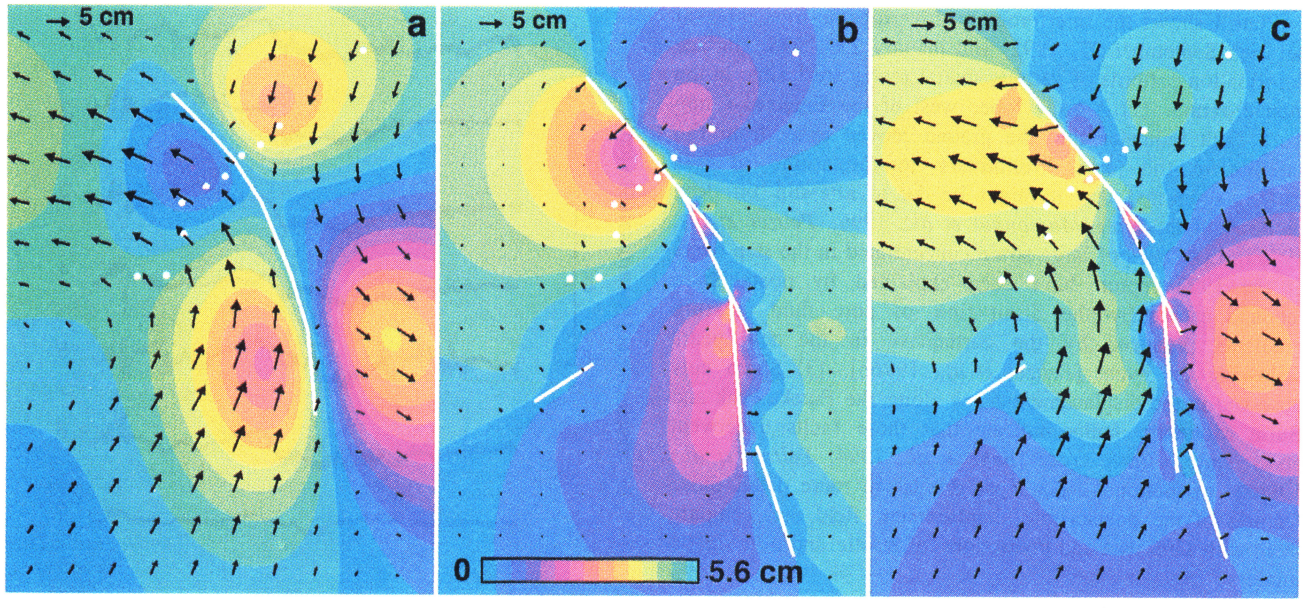

Plate 2. Surface displacement predicted by (a) *Savage and Svarc*'s [1997] afterslip model, (b) poroelastic model, and (c) the combination of models in Plates 2a and 2b. One color cycle represents 5.6 cm of surface displacement toward radar. Black arrows depict horizontal displacement vectors. White lines show fault geometry of *Savage and Svarc*'s[1997] afterslip model (Plate 2a) and of *Wald and Heaton*'s [1994] coseismic model (Plates 2b and 2c). White dots are locations of GPS stations used by *Savage and Svarc* [1997]. Models are scaled as in Figure 4a to represent surface displacement during time interval spanned by SAR data shown in Figure 4a.

3.1.1. Comparison between SAR data, GPS data, and afterslip model. To compare the displacements measured by GPS along the transect across the Emerson-Camp Rock fault (diamonds in Plate 1) with the SAR data (profile 1, Plate 1), we projected onto the radar line of sight both the horizontal and vertical components of the GPS-estimated vectors [*Savage and Svarc* , 1997, Table 1 and Figure 6b] after appropriate scaling for matching the observation time period of the SAR data (Figure 4a). Unfortunately, this comparison appeared to be meaningless because of the quite large error bars of the vertical displacement rate estimates in the GPS data. Because the ERS SAR line of sight incidence angle at midswath is 23° off the vertical, the ±12 mm/yr error bars on the vertical rates obtained with the GPS lead to ±5 cm of error in range change over the 4 years of observation with the SAR, an error that is larger than the largest signal observed along the profile in the SAR data (Figure 4a). The line of sight projection of the horizontal components of GPS vectors, however, seems to be in agreement with the SAR range change in the far field, but a large discrepancy between the two data sets occurs within 10 km from the fault, where vertical motion is likely to have taken place.

Savage and Svarc [1997] interpreted the signal seen with seven surveys of the GPS array in the first 3.4 years after the earthquake as being caused by right-lateral afterslip on the downward projection of the 1992 rupture plane between depths of 10 and 30 km. The preferred afterslip solution (model A) of *Savage and Svarc* [1997] implies up to 1 m of slip on the Emerson section of the fault. A comparison between the line of sight surface displacement observed in the SAR data and that predicted by this model shows evident inconsistency (Figure 4b and Plate 2a). In the area west of the Emerson-Camp Rock fault the SAR data show a range increase (movement away from the satellite) (Figure 3 and Plate 1) and the afterslip model predicts a range decrease (movement toward the satellite) (Plate 2a). Along the GPS transect line, the observed and modeled range displacement profiles have opposed polarities: the SAR data indicate a range increase west of the fault and a range decrease east of it; the model predicts the opposite. Figure 4b also shows the independent contributions to the range change profile of the vertical and horizontal components of the displacement predicted by the model. It is clear that the line of sight displacement is dominated by the vertical surface motion, a contribution that is ignored in *Savage and Svarc*'s [1997] inversion because of the poor accuracy of the GPS data in the vertical.

3.1.2. Poroelastic rebound. If afterslip has to be advocated to explain the right-lateral shear parallel to the fault observed in the GPS horizontal displacement vectors [*Savage and Svarc*, 1997], one has to explain why the contribution of the vertical motion predicted by the model is not depicted in the SAR data. A possible way of reconciling afterslip models and SAR observations is to advocate poroelastic rebound due to pore fluid flow in the shallow crust. As in the fault step overs [*Peltzer et al.*, 1996b], the volume of rocks adjacent to the fault undergoes compression or stretching during the earthquake. This strain results in small volume changes and generates pore fluid pressure gradients in the shallow crust. As time passes after the earthquake, fluid flow allows pore pressure gradients to dissipate, and the volume of rock eventually reaches a drained condition. Theoretical models of elastic media containing holes [e.g., *MacKenzie*, 1950; *Sato*, 1952] and laboratory experiments on a wide variety of crustal rocks [e.g., *Rice and Cleary*, 1976] indicate that the Poisson's ratio of a porous media under undrained conditions (coseismic) is larger than its value under drained conditions (postseismic).

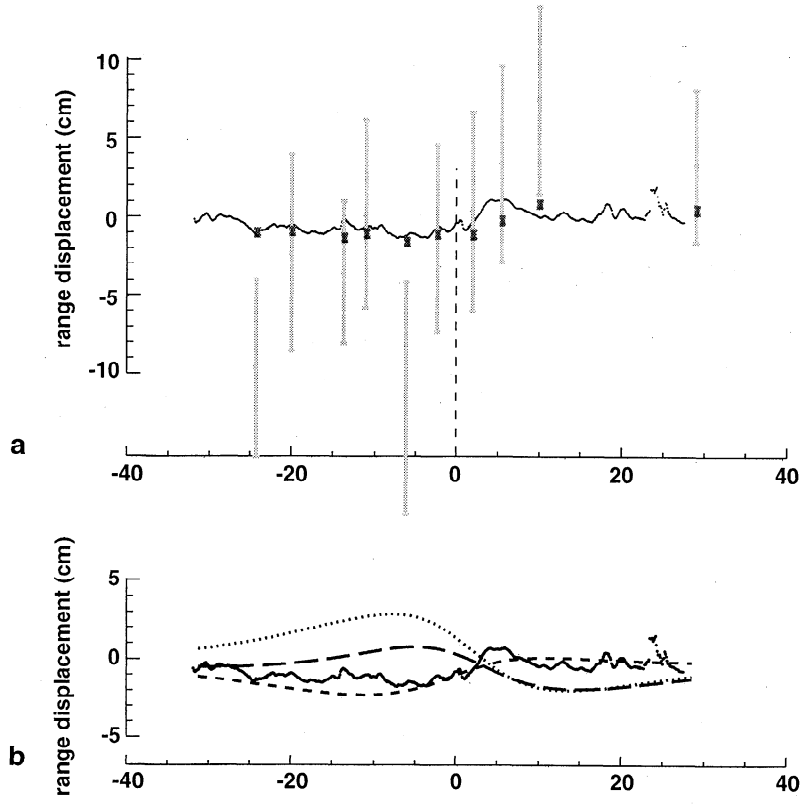

Figure 4. (a) Comparison of range change along profile 1 between August 7, 1992, and September 24, 1995, observed in SAR data (solid line) with surface displacement estimated with GPS measurements along Emerson fault transect [*Savage and Svarc*, 1997]. Light gray dots and bars are projections of three components of GPS vectors and 1σ error bars along radar line of sight. Dark gray dots and bars are projection of GPS vectors horizontal components only. GPS data are scaled to match time interval covered by radar data the following way: horizontal components [*Savage and Svarc*, 1997, Table 1] are scaled by [*f*(s2)-*f*(s1)]/[*f*(t2)-*f*(t1)], where *f* is temporal function describing postseismic GPS displacement [*Savage and Svarc*, 1997], t1 and t2 are epochs of first and last GPS survey of transect and s1 and s2 are epochs of SAR passes for data shown; GPS uplift rates [*Savage and Svarc* , 1997, Figure 6] are scaled by (s2-s1). Origin is arbitrary along range displacement axis. (b). Line of sight displacement observed in SAR data (solid line) compared with range change predicted by *Savage and Svarc*'s [1997] model A (long dashes) along profile 1 (Plate 1). Dotted (respectively short dashed) line shows independent contribution of vertical (respectively horizontal) component of surface displacement predicted by model to range change displacement. Modeled curves are scaled as GPS data in Figure 4a.

Hence the postseismic relaxation of pore fluid pressure gradients induced by the coseismic volume change of the country rock produces a rebound phenomenon. In the case of a strike-slip dislocation, vertical displacements are essentially proportional to the Poisson's ratio of the elastic crust, and poroelastic effects are expected to be large in the vertical component of the postseismic displacement field.

The constitutive relation describing a fluid-infiltrated, poroelastic material is the same under undrained (no fluid flow) and drained (constant pore pressure) conditions, provided that the correct value of the Poisson's ratio (drained or undrained) is used. However, the same shear modulus applies to both cases [*Biot*, 1956; *Roeloffs*, 1996]. We simply modeled the poroelastic rebound subsequent to the Landers earthquake by computing the difference between two coseismic dislocation models [*Okada*, 1985], using undrained and drained values of the Poisson's ratio. We used the fault geometry and coseismic slip distribution of the joint inversion model of *Wald and Heaton* [1994] to predict the poroelastic rebound (Plate 2b). Using values of ν_d=0.27 and ν_u=0.31 for the drained and undrained Poisson's ratio, respectively [*Rice and Cleary*, 1976], the combination of this rebound and the range change predicted by *Savage and Svarc*'s [1997] model A results in a range change profile bearing the same polarity and comparable amplitude as the range change profile observed in the SAR data (Figures 5a and Plate 2c). One has to note that the Poisson's ratio values used in the elastic model represent average values over the depth of ~15 km (the depth of the modeled dislocation) of parameters that vary with depth.

However, this combined model produces a steep gradient in the profile closer to the fault than it is observed in the SAR data. In the observed profiles, the gradient occurs between 1 and 5 km east of the 1992 surface break (Figures 3, 5a). A possible reason to explain the observed shifted location of the steep gradient is that the 1992 surface break has two branches, just north of the studied profile, suggesting that the actual shear may have occurred at depth slightly east of the surface break where the profile intersects with the fault. Because the poroelastic rebound is directly derived from a model representing the Emerson-Camp Rock fault as a vertical.

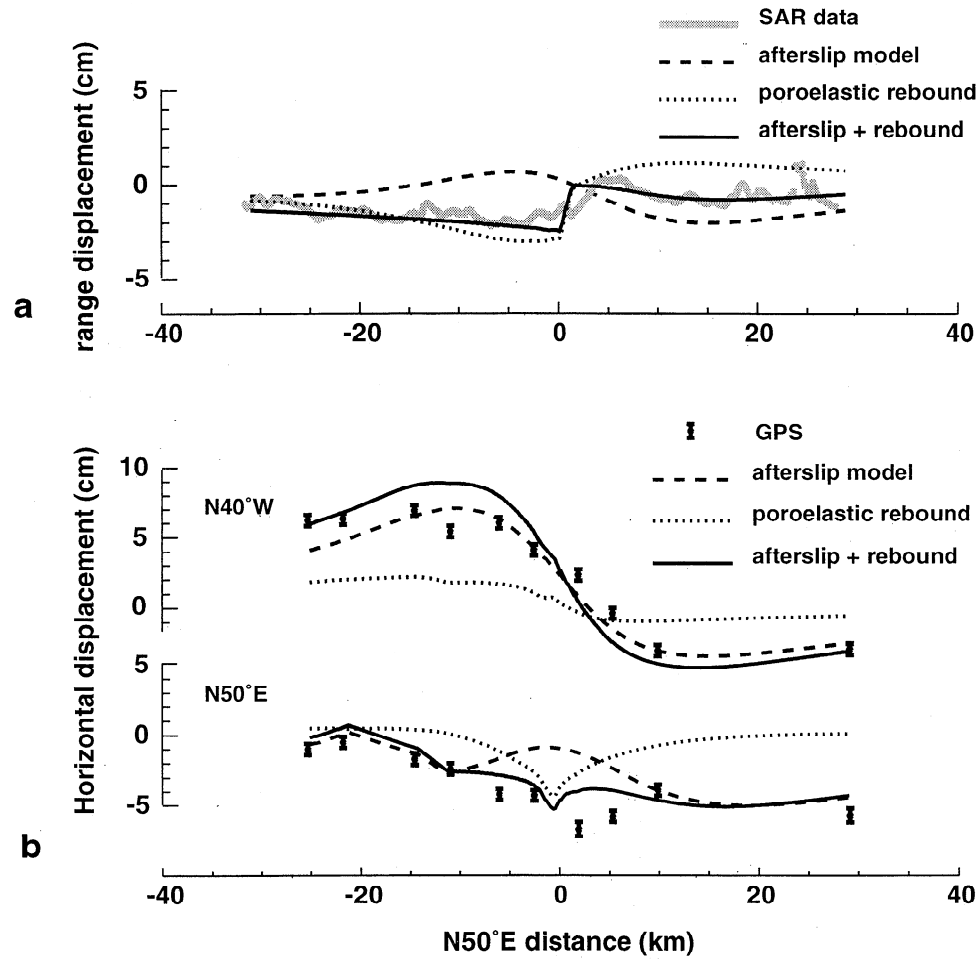

Figure 5. (a) Observed (gray) and modeled (black) range displacement along profile 1 (Plate 1). Dashed line is *Savage and Svarc*'s [1997] afterslip model. Dotted line is poroelastic rebound model. Black, solid line is the sum of the two. (b) Comparison of observed N50°E and N40°W displacement at GPS stations in the Landers array with that predicted by *Savage and Svarc*'s [1997] afterslip model (dashed lines), the poroelastic rebound (dotted lines), and the combination of the two (solid lines) plotted as a function of the N50°E distance from the rupture trace. Error bars on GPS data are 1σ. Modified from *Savage and Svarc* [1997].

straight fault segment [*Wald and Heaton*, 1994], such complexities of the fault geometry and near-field displacements are not taken into account in the present poroelastic model.

Another important feature of the poroelastic rebound model is the significant horizontal displacement occurring near the fault along the Emerson-Camp Rock segment (Plate 2b). This horizontal rebound is similar to the vertical rebound discussed above and has important geodetic implications. Any strike-slip dislocation in an elastic half-space produces a surface displacement field with four characteristic lobes. In the case of the Landers earthquake, the volume of rock in the northwest quadrant, west of the Emerson-Camp Rock fault, experienced horizontal compression during the earthquake and expanded both vertically and horizontally, perpendicular to the fault direction. By contrast, the volume of rock in the northeast quadrant, east of the Emerson-Camp Rock fault, experienced horizontal extension during the earthquake and shrank both vertically (subsidence) and horizontally, perpendicular to the fault. The combined effects of the compression west of the fault and the extension east of it resulted in particular in an east-northeast shift of the ground in the vicinity of the fault during the earthquake. Because this horizontal shift is proportional to the Poisson's ratio of the elastic crust, the poroelastic process discussed above produces a postseismic, horizontal shift of the ground near the Emerson fault in the opposite direction (Plate 2b). A symmetric pattern is observed along the southern branch of the 1992 dislocation, where poroelastic rebound implies a fault-perpendicular, eastward movement of the surface near the Johnson Valley fault (Plate 2b).

It is interesting to note that the fault-perpendicular component of the displacement field, a feature that is not explained by the afterslip model alone, may account for the discrepancy between the afterslip model proposed by *Savage and Svarc* [1997] and the GPS data in the N50°E component. Notably, the poroelastic rebound produces a negative notch in the N50°E displacement component profile that is qualitatively similar to the fault-perpendicular motion observed in the GPS data near the fault (Figure 5b). A quantitative agreement between the observed and modeled N50°E profiles would require a coseismic slip distribution on

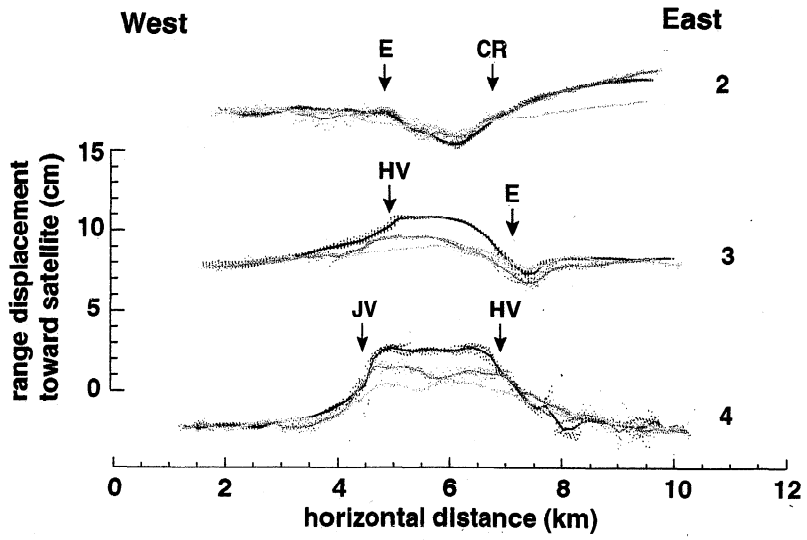

Figure 6. Line of sight surface displacement along profiles 2, 3, and 4 shown in Plate 1 observed in interferograms spanning August 7, 1992, to September 24, 1995 (black), September 27, 1992, to January 23, 1996 (dark gray), and January 10, 1993, to May 25, 1995 (light gray), time intervals. Dots are displacement of individual image pixels within 400 m from profile line, and solid curves indicate averaged values in 160-m-long bins along profiles strike. Arrows indicate locations of faults. Fault labels are E, Emerson fault; CR, Camp Rock fault; HV, Homestead Valley fault; and JV, Johnson Valley fault. After *Peltzer et al.* [1996b].

shallow fault patches different from that in *Wald and Heaton*'s [1994] solution that is used here to compute the poroelastic rebound. In addition, the poroelastic model also predicts a small component of right-lateral shear parallel to the Emerson Camp Rock fault (Figure 5b). This suggests that by having not taken into account poroelastic effects, *Savage and Svarc*'s [1997] solution may be an overestimate of the amount of deep afterslip by ~30%.

Finally, it is important to note the failure of the combined model to predict the observed range change along the southern half of the 1992 break. As in the northern half of the modeled displacement field, the afterslip model produces two large lobes on both sides of the Johnson Valley fault (Plate 2a). The range displacement predicted by the poroelastic rebound model (Plate 2b) compensates partially the lobed pattern west of the fault and only marginally that east of the fault (Plate 2c). The resulting displacement pattern differs markedly from the observed range change in this area (Plate 1). The SAR data show a region of range decrease west of the fault and a relatively flat signal east of it. In the absence of ancillary geodetic data in this area, we may tentatively argue that the amount of afterslip along the southern branch of the 1992 rupture may be greatly overestimated in *Savage and Svarc*'s [1997] solution.

3.1.3. Viscoelastic relaxation. An alternative explanation that would also reconcile the right-lateral shear observed in the GPS horizontal vectors with the SAR observations is that the shear could result from viscoelastic relaxation in the lower crust/upper mantle layers rather than from deep afterslip on the fault. Recent developments of two-layer models have shown that vertical movements of the surface during postseismic relaxation can be negligible compared to horizontal movements when gravity is taken into account [*Yu et al.*, 1996; *Pollitz*, 1997]. Such models might then explain the fault-parallel shear observed in the GPS data without producing the vertical displacement quadripole pattern that is characteristic of strike-slip dislocations, yet not observed in the SAR data. However, viscoelastic relaxation is generally associated with time constants longer than the duration of our observations and hence may have little influence during the first 4 years after a large earthquake. Furthermore, the steep gradient in range change observed near the 1992 rupture requires a relatively shallow source; this feature cannot be accounted for by viscoelastic relaxation in the lower crust, as it would lead to much broader and smoother surface displacement patterns [*Yu et al.*, 1996; *Pollitz*, 1997]. A critical test of the viscoelastic hypothesis would be to characterize the time dependence of the long-term postseismic displacement processes using geodetic observations covering a decade after the 1992 event.

3.2. Poroelastic Rebound in the Homestead Valley Fault Step Over

We have proposed that the intense surface strains observed in the interferograms in the step overs of the 1992 surface rupture were attributable to the poroelastic response of the shallow crust to coseismic strain [*Peltzer et al.*, 1996b]. In this section we develop a model based on a dislocation in an elastic half-space to quantify such rebound in the Homestead Valley pull-apart structure and discuss implication of this model on the seismic velocity structure of the fault zone.

In the pull-apart basins between the Homestead Valley and Johnson Valley faults and between the Emerson and Homestead Valley faults, the observed ground displacement produced range decreases, consistent with surface uplift (Plate 1 and Figure 6). In the compressive jog between the Camp Rock and Emerson faults, the observed displacement produced range increase, consistent with ground subsidence (Plate 1 and Figure 6). Analysis of several interferograms covering various time intervals within the 4 years after the earthquake indicates that the decay time associated with this process is 0.75 ± 0.12

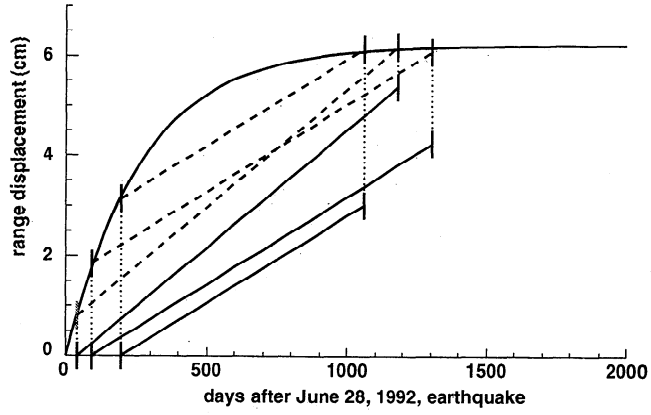

Figure 7. Postseismic uplift in Homestead Valley pull apart plotted as a function of time. Curve is function $w(t) = w_0(1-e^{-t/\tau})$, adjusted to data ($w_0$=6.2 cm, τ=0.75 years). Solid lines are uplift estimates using SAR data of profile 4 (Figure 6). Vertical bars indicate ±0.5 cm error on uplift estimates. Dashed lines are same as solid lines, shifted to match adjusted curve $w(t)$.

years (Figure 7), similar to the characteristic time describing earthquake-associated phenomena that are often explained by pore fluid flow in the upper crust [*Nur and Booker*, 1972; *Booker*, 1974; *Anderson and Whitcomb*, 1975; *Li et al.*, 1987; *Muir-Wood and King*, 1993]. These observations led us to propose that the postseismic rebound signal observed in fault step overs was due to changes in mechanical properties of the shallow crustal rocks in the fault zone, as pore pressure gradients caused by the earthquake dissipated [*Peltzer et al.*, 1996b].

Using the same approach as for the Emerson-Camp Rock fault, we modeled the poroelastic rebound in the Homestead Valley pull-apart structure by computing the difference between two elastic dislocation models based on a coseismic slip distribution and using different values of the Poisson's ratio, corresponding to the undrained (coseismic) and drained (postseismic) conditions. A more realistic fault geometry and slip distribution than that modeled in *Wald and Heaton*'s [1994] global solution was necessary to take into account the local complexity of the displacement field in the pull-apart structure. The fault model includes 1-2-km-long, 4-km-deep, vertical fault patches aligned with the fault traces along the Homestead Valley, the Kickapoo, and the Johnson Valley sections of the 1992 surface rupture [*Sieh et al.*, 1993]. The horizontal, coseismic slip for each patch was then interpolated between the data points mapped by *Sowers et al.* [1994] from latitude 34.28°N to 34.37°N and by *Sieh et al.* [1993] and *Hart et al.* [1993] for the southern section of the Johnson Valley fault and the northern section of the Homestead Valley fault (Plate 3). The "slip gap" section in the southern Homestead Valley fault where no surface offset was observed in the field [*Sieh et al.*, 1993; *Spotila and Sieh*, 1995] has been assigned a slip of 1 m based on the *Hudnut et al.* [1994] coseismic slip model.

The areal distribution of predicted surface uplift agrees reasonably well with the SAR observations (Plates 1 and 3). As expected, the model predicts surface uplift in the valley between the overlapping sections of the 1992 rupture (Plate 3). The model also predicts surface uplift near the bend in the Johnson Valley fault (latitude 34.26°N, Plate 3). Postseismic motion there may result from coseismic strain of the adjacent volume of rock due to curvature of the fault and the large along-strike variation of coseismic slip in this section of the fault (Plate 3). However, the model also predicts range decrease east of the Homestead Valley fault near the northern tip of the Kickapoo fault (Plate 3), an area where no such displacement is observed in the SAR data (Plate 1). Improper modeling of the fault geometry and slip at depth along this complicated section of the 1992 rupture [e.g., *Spotila and Sieh*, 1995] is the most likely explanation for the model's failure in this area.

Figure 8 shows the observed and predicted slant range components of displacement along the profile across the Homestead Valley pull apart (Plate 1) using two sets of Poisson's ratios values. First, we have assumed values 0.27 and 0.3 for the drained and undrained Poisson's ratios of the shallow rocks, respectively [*Rice and Cleary*, 1976; *Li et al.*, 1992; *Peltzer et al.*, 1996b]. These values imply a postseismic rebound accounting for less than 2 cm of range change in the pull apart. A greater contrast between undrained and drained Poisson's ratio values would be needed to account for the observed displacement in the SAR data.

Recent seismological studies have revealed abnormally low S wave velocities and correspondingly high V_p/V_s ratios within fault zones at shallow depth [e.g., *Michelini and McEvilly*, 1991; *Li et al.*, 1997]. Reports on fault zone guided waves from near-surface explosions in the San Andreas fault at Parkfield indicate values of up to 2.5 for the V_p/V_s ratio in the upper 3 km of the fault zone [*Li et al.*, 1997; Y.G. Li, personal communication, 1997]. Such low values contrast with crustal

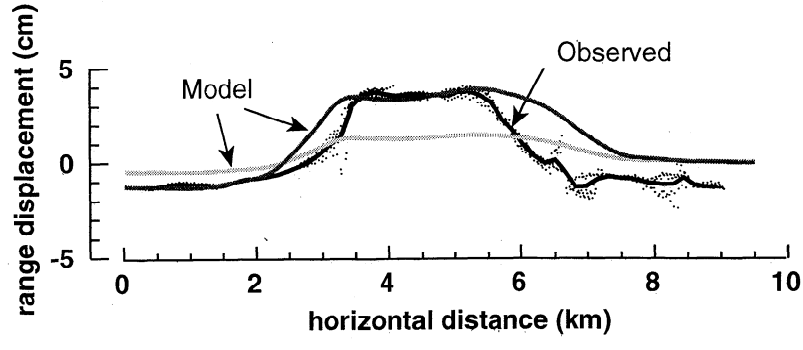

Figure 8. Observed and predicted line of sight displacement along profile 4 (Plate 1) across Homestead Valley pull-apart structure for the August 7, 1992, to September 24, 1995, time period. Light shade and dark shade modeled profiles correspond to sets of drained/undrained Poisson's ratios of 0.27/0.30 and 0.27/0.35, respectively.

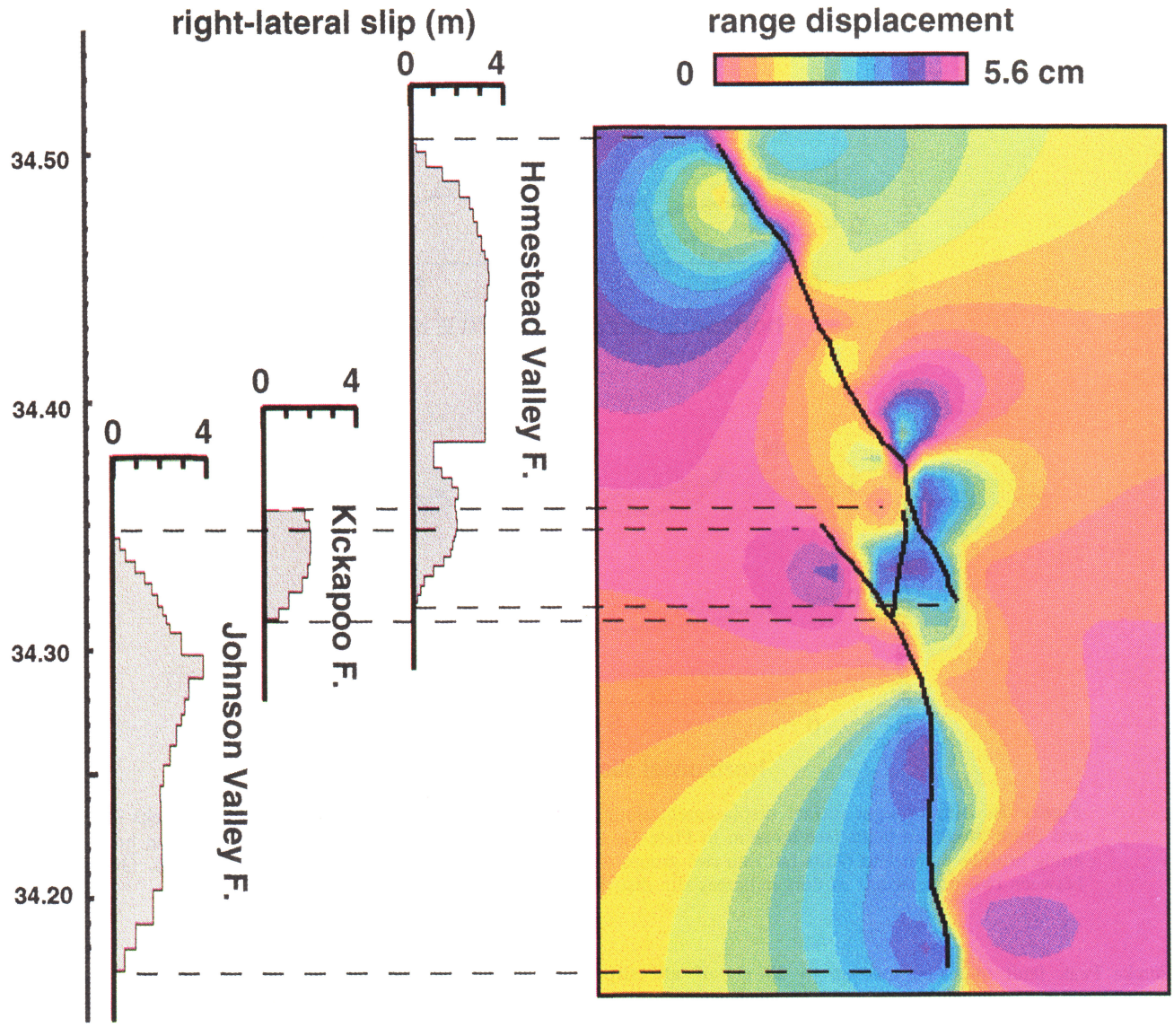

Plate 3. Modeled line of sight surface displacement resulting from poroelastic rebound in the Homestead Valley pull-apart structure. Elastic model is based on coseismic fault slip distribution shown on the left. Slip data are after *Sowers et al.* [1994], *Sieh et al.* [1993], *Hart et al.* [1993], and *Hudnut et al.* [1994].

velocity values estimated for the overall Mojave block [e.g., *Li et al.*, 1992] and are commonly attributed to intense fracturing, brecciation, and fluid saturation of gouge rocks within the fault zones. Because the undrained Poisson's ratio is directly related to the ratio of seismic waves velocities V_p/V_s according to

$$\frac{V_p}{V_s} = \sqrt{2\frac{1-\nu_u}{1-2\nu_u}}, \quad (1)$$

a large V_p/V_s ratio indicates a large value of the undrained Poisson's ratio. In particular, V_p/V_s = 2.5 implies ν_u = 0.4. Using the value of 0.35 for the undrained Poisson's ratio, within the range discussed by *Li et al.* [1997] for a brecciated fault zone, and a value of 0.27 for the drained Poisson's ratio [*Rice and Cleary*, 1976], the model leads to a poroelastic induced range decrease of ~5 cm in the Homestead Valley pull apart, in good agreement with the displacement observed in the SAR data (Figure 8). This result supports our earlier interpretation that pore fluid flow provides a plausible mechanism to account for the observed surface movements in the fault step overs after the Landers 1992 earthquake [*Peltzer et al.*, 1996b]. It is interesting to note that with the large value of 0.35 for the undrained Poisson's ratio, the dislocation model predicts a coseismic subsidence of ~20 cm in the Homestead Valley pull-apart structure, consistent with subsidence measured by leveling before and after the earthquake (A. Sylvester, personal communication, 1996).

3.3. Surface Creep Along the Burnt Mountain and Eureka Peak Faults

Sharp discontinuities in the displacement field are readily visible in the interferograms along the Burnt Mountain and the Eureka Peak faults' 1992 surface breaks (Plate 1 and Figure 9a). These features result from fault creep occurring in the years following the earthquake. Creep meters installed along the

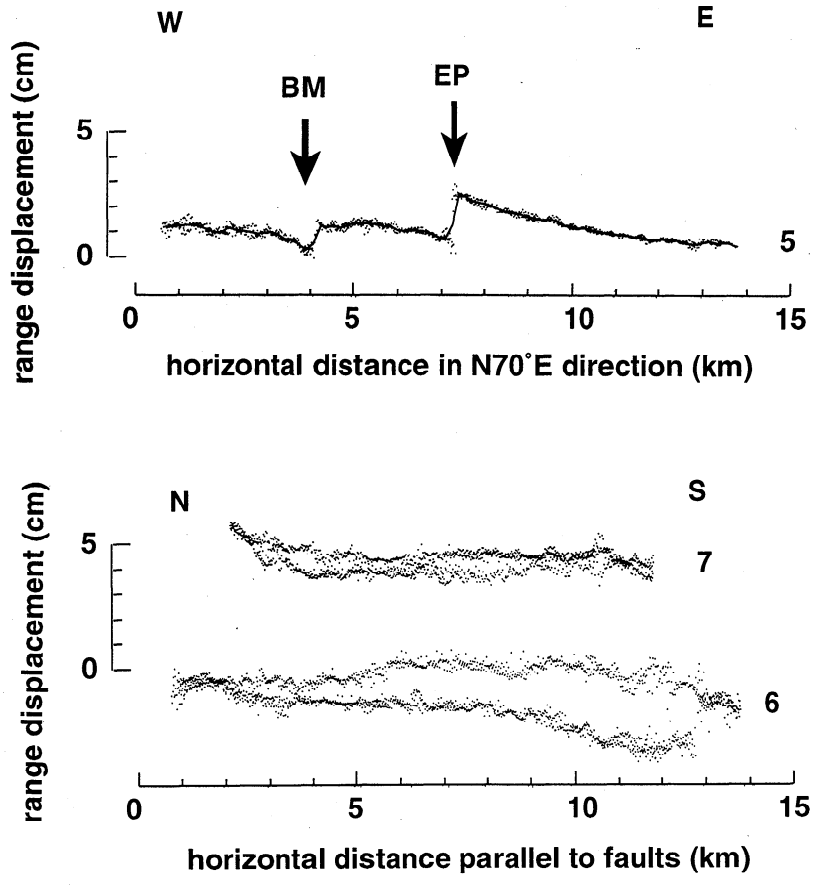

Figure 9a. Line of sight surface displacement along profiles across (5) and parallel to (6 and 7) Eureka Peak and Burnt Mountain faults (see location in Plate 1). Displacement values of individual image pixels in boxes along profiles parallel to faults fall into two groups depending on pixel location with respect to faults. Offset between two populations of dots indicates slip distribution along faults.

Eureka Peak fault indicated that up to 23 cm of afterslip occurred on the Eureka Peak fault in the first year following the earthquake [*Behr et al.*, 1994]. No instrument was installed on the Burnt Mountain fault, and postseismic creep had not previously been recognized along this fault to our knowledge. The phase profile across the creeping sections of the two faults indicates that afterslip is limited to shallow patches on the faults (Figure 9a). In fact, the distance from the faults over which the displacement vanishes does not exceed 5 km for the Eureka Peak fault and 2 km for the Burnt Mountain faults, corresponding to downdip widths of the creeping patches of ~3 km and ~1 km, respectively. The box profile parallel to the Burnt Mountain fault shows that creep is nearly uniformly distributed along the 9-km-long creeping section of that fault and it produced ~1-1.5 cm of line of sight displacement. If the observed offset is due to purely horizontal slip on the north-

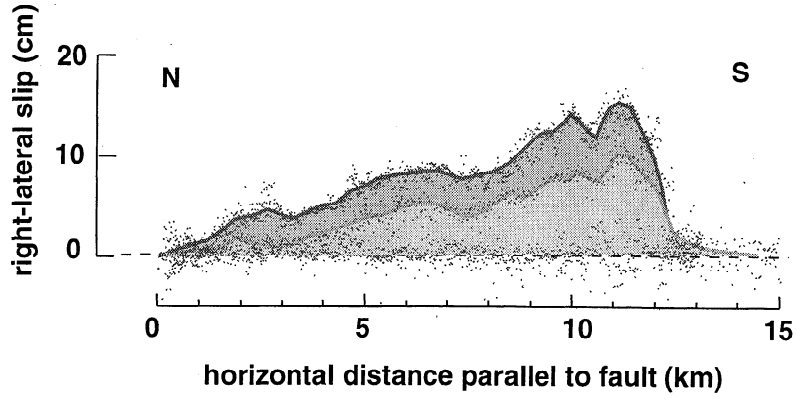

Figure 9b. Postseismic slip distribution observed along Eureka Peak fault for time intervals September 27, 1992, to January 23, 1996 (top curve), and January 10, 1993, to May 23, 1995 (bottom curve). Right-lateral component of slip is derived from line of sight displacement assuming purely horizontal, strike-slip movement on fault.

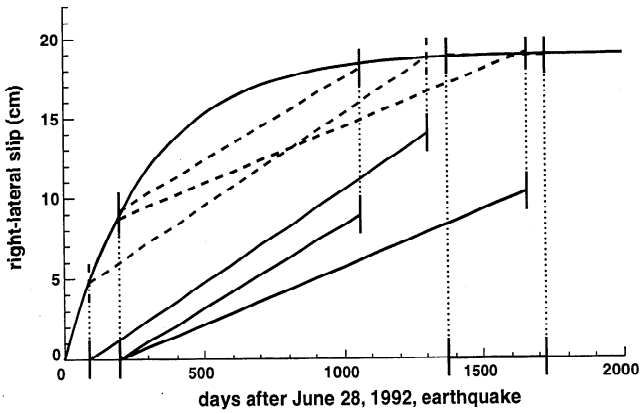

Figure 10. Same as Figure 7 for afterslip data along Eureka Peak fault. Exponential curve fit to data indicates a relaxation time of 0.8 years.

south striking fault, the observed change corresponds to 12-17 cm of right-lateral slip for the observation period spanned by the data. The box profile parallel to the Eureka Peak fault indicates that slip gradually increases from north to south and abruptly stops near the southern end of the 1992 surface rupture (Figure 9a). Figure 9b shows the slip distribution along the creeping section of the Eureka Peak fault for the September 27, 1992, to January 23, 1996, and January 10, 1993, to May 23, 1995, time periods, assuming the observed range change corresponds to purely horizontal strike slip on the N160°E striking fault [*Behr et al.*, 1994; A. Sylvester, personal communication, 1996]. If the observed slip is distributed uniformly over a depth of ~3 km, the along-strike slip distributions shown in Figure 9b correspond to geodetic moments of 9.3 x 10^{16} N m and 5.4 x 10^{16} N m for the two time periods, respectively. It is interesting to note that the cumulative seismic moments released by aftershocks within 5 km from the Eureka Peak fault during the same time periods over the entire seismogenic depth are only 9.0 x 10^{14} and 1.6 x 10^{14}, respectively, more than 2 orders of magnitude lower than the geodetic moments above.

The proportionality of slip distributions for the two intervals shown in Figure 9b indicates a consistent temporal behavior of the slip rate distribution along strike. Using data covering four time intervals between September 1992 and March 1997, we have adjusted an exponential function of the type

$$w = w_0(1 - e^{-t/\tau}) \tag{2}$$

to the observed afterslip and derived a characteristic time of 0.8 years (0.55 years < τ < 1.3 years) (Figure 10). As with the decay time associated with the postseismic rebound in the fault step overs, a decay time of 0.8 years also suggests a possible dependence on fluid flow in the shallow crust. Recent studies have emphasized the role of fluids in explaining the behavior of seismic and creeping faults [e.g., *Rudnicki and Chen*, 1988; *Blanpied et al.*, 1992; *Sleep and Blanpied*, 1992; *Lockner and Byerlee*, 1994; *Sleep and Blanpied*, 1994]. Following these studies, we propose a scenario involving dilatant hardening followed by pore pressure controlled creep to explain the shallow afterslip observed along the Eureka Peak fault. Frictional slip is often accompanied by dilatancy, causing a local pore pressure decrease and an increase in the effective normal stress on the fault plane, thus inhibiting further slip [*Rudnicki and Chen*, 1988]. If such a mechanism (dilatant hardening) is responsible for the locking of the shallow part of the Eureka Peak fault during the 1992 earthquake, the following conditions should exist immediately after the earthquake: (1) a residual shear stress equivalent to a quantity of slip D is stored as elastic strain in the country rock over a distance L on each side of the fault (Figure 11), (2) the local pore pressure is below hydrostatic equilibrium. As pore fluid flow gradually restores hydrostatic pressure in the fault zone, the effective normal stress is reduced on the fault and creeping begins. As creep goes on, the Coulomb criterion

$$\tau = \tau_0 + C(\sigma_n - p_f) \tag{3}$$

expresses the relation between the shear stress τ and normal stress σ_n on the fault plane, and the local pore pressure p_f. Slip on the fault causes the shear traction to decrease as the postseismic displacement d increases according to

$$\tau = \mu \frac{D - d}{L} \tag{4}$$

where μ is the elastic shear modulus of the adjacent rocks (Figure 11). If we assume that the normal stress remains constant during the time period of observation, equations (3) and (4) show that d and p_f are linearly related and should therefore have the same time dependence. If the temporal behavior of the pore pressure after the earthquake is described by an exponential increasing function, the postseismic displacement d must increase similarly with time. By gradually reducing the effective normal stress on the fault, the pore pressure increase controls the creep rate on the fault.

4. Conclusion

We have analyzed intermediate- and near-field, postseismic surface displacements following the Landers 1992 earthquake using ERS-1 SAR data covering various time intervals between September 1992 and March 1997. The interferometric maps revealed transient displacement patterns of various spatial scales that were either not observed or only partially captured by other geodetic techniques. In particular, the SAR maps depict clearly vertical displacements of the ground surface, a component of the displacement field that has been ignored in previous studies using other geodetic measurements. Analysis

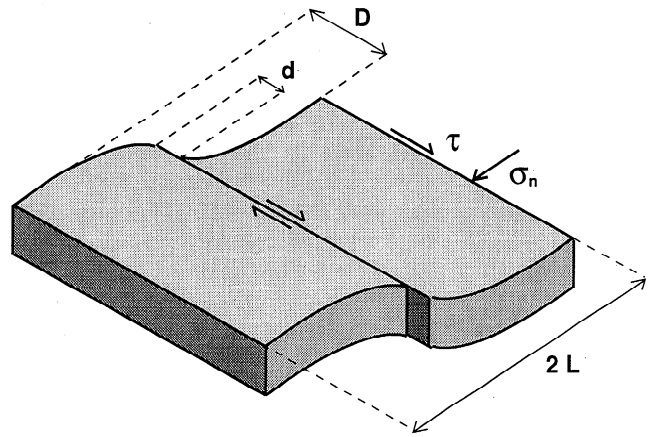

Figure 11. Three-dimensional sketch of creeping fault defining parameters D, d, τ, σ_n, and L discussed in text.

of the range change maps covering 4 years after the 1992 earthquake suggests that poroelastic rebound, resulting from the change of the Poisson's ratio value of the strained rocks from undrained to drained conditions as pore fluid flow allows pore pressure gradients caused by the earthquake to dissipate, occurred not only in the fault step overs of the 1992 rupture [*Peltzer et al.*, 1996b] but also at distances of up to 15 km from the fault, an area where the country rock experienced large pore volume changes during the earthquake.

Our combined analysis of SAR data and GPS data from the Emerson-Camp Rock fault array indicates that afterslip models alone cannot account for the observations because they would produce vertical displacement patterns that are not observed in the SAR data. We show that the added effects on the displacement field of poroelastic rebound caused by pore fluid flow and afterslip on deep sections of the fault can account for the observed displacements near the Emerson-Camp Rock fault in both the radar line of sight and the horizontal directions. In particular, the analysis shows that, when combined with poroelastic rebound, the afterslip model of *Savage and Svarc* [1997] overestimates the amount of slip by ~30% on the Emerson-Camp Rock fault. The combined model, however, fails to explain the range change pattern observed along the southern half of the 1992 surface break.

Forward modeling of the poroelastic rebound previously recognized in the Homestead Valley-Johnson Valley faults pull-apart structure [*Peltzer et al.*, 1996b] requires a large undrained Poisson's ratio value (ν_u = 0.35) to successfully account for the observed postseismic uplift in the pull apart. High values of ν_u are independently suggested by the observed, abnormally low *S* wave velocities in the upper 3-5 km of fault zones, where values as high as 2.5 have been estimated for the V_p/V_s ratio of fault zone guided waves [*Li et al.*, 1997].

Finally, SAR interferometric maps revealed that two sections of the 1992 rupture, the Eureka Peak fault and the Burnt Mountain fault, have undergone surface creep in the years following the earthquake. Clear cuts in the displacement field aligned with the fault traces allowed us to map the along-strike surface-slip distribution along these two faults. A simple model, involving dilatant hardening (fault locking process) followed by pore pressure controlled effective normal stress release, is proposed to explain the similarity between the observed decay time of fault creep and the relaxation times that describe percolation of fluids in the shallow crust. Along the Eureka Peak fault, the geodetic moment released by shallow afterslip exceeds the cumulative seismic moment released by aftershocks in the vicinity of the fault over the entire seismogenic depth during the same time periods by more than 2 orders of magnitude.

The spatial scale of the most intense postseismic deformation features observed in the radar interferograms ranged from a hundred meters to a few kilometers. Such a scale range is typically too small to be observed by GPS [e.g., *Shen et al.*, 1994] and too large to be detected by small aperture trilateration arrays across the fault [*Sylvester*, 1993]. Except along the Eureka Peak fault where creep has been monitored in three places during the year after the earthquake [*Behr et al.*, 1994], most of the near-field, postseismic deformation observed in the SAR data has been missed by the ground-based geodetic techniques. Furthermore, it has been possible to detect the various effects of postseismic fluid flow because of the great sensitivity of SAR measurements to vertical displacements of the ground, a component that was poorly estimated, or not estimated at all, by other geodetic techniques used after the Landers earthquake.

These remarks emphasize the importance of measuring the three components of the surface displacement field continuously in space along active faults susceptible of generating earthquakes. If measurable precursory transient processes ever occur before some earthquakes, as it has been proposed in several instances [e.g., *Allen et al.*, 1991; *Kanamori and Anderson*, 1975; *Linde et al.*, 1988; *Shifflett and Whitboard*, 1995; *Thurber*, 1996], the associated ground movements may have remained undetected because of the inherent limitations of available geodetic techniques. In that sense, SAR interferometry has a great potential to efficiently complement point positioning geodetic techniques in the study of earthquakes and related processes.

Acknowledgments. We would like to thank E. Ivins and Y.G. Li for helpful discussions, W. Thatcher for his comments on an early version of the manuscript, and C.Y. Wang, H. Zebker, and D. Massonnet for their reviews. The ERS radar data were provided by the European Space Agency. The work presented in this paper has been performed at the Jet Propulsion Laboratory, California Institute of Technology under contract with NASA.

References

Allen, C.R., Luo Z., Qian H., Wen X., Zhou H., and Huang W., Field study of a highly active fault zone: The Xianshuihe fault of southwestern China, *Geol. Soc. Am. Bull.*, *103*, 1178-1199, 1991.

Anderson, D.L., and J.H. Whitecomb, Time-dependant seismology, *J. Geohys. Res.*, *80*, 1497-1503, 1975.

Behr, J., R. Bilham, P. Bodin, and S. Gross, Eureka Peak fault afterslip following the 28 June 1992 Landers earthquake, *Bull. Seismol. Soc. Am.*, *84*, 826-834, 1994.

Biot, M. A., General solutions of the equations of elasticity and consolidation for a porous material, *J. Appl. Mech.*, *23*, 91-96, 1956.

Blanpied, M.L., D.A. Lockner, and J.D. Byerlee, An earthquake mechanism based on rapid sealing of faults, *Nature*, *358*, 574-576, 1992.

Bock, Y., et al., Southern California permanent GPS geodetic array: Continuous measurements of regional crustal deformation between the 1992 Landers and 1994 Northridge earthquakes, *J. Geophys. Res.*, *102*, 18,013-18,034, 1997.

Booker, R.J., Time dependent strain following faulting of porous medium, *J. Geophys. Res.*, *79*, 2037-2044, 1974.

Delacourt, C., P. Briole, and J. Achache, Tropospheric correction of SAR interferograms with strong topography. Application to Etna, *Geophys. Res. Lett.*, in press, 1998.

Dokka, R.K., and C.J. Travis, Late Cenozoic strike-slip faulting in the Mojave Desert, California, *Tectonics*, *9*, 311-340, 1990.

European Space Agency, ERS-1 system, 87 pp., ESA Publ. Div., Eur. Space Res. and Technol. Cent., Noordwijk, Netherlands, 1992.

Feigl, K., A. Sergent, and D. Jacq, Estimation of an earthquake focal mechanism from a satellite radar interferogram: Application to the December 4, 1992 Landers aftershock, *Geophys. Res. Lett.*, *22*, 1037-1040, 1995.

Gabriel, A.G., R.M. Goldstein, and H.A. Zebker, Mapping small elevation changes over large areas: Differential radar interferometry, *J. Geophys. Res.*, *94*, 9183-9191, 1989.

Gill, A.E., *Atmosphere-Ocean Dynamics*, 662 pp., Academic, San Diego, Calif., 1982.

Goldstein, R., Atmospheric limitations to repeat-track radar interferometry, *Geophys. Res. Lett.*, *22*, 2517-2520, 1995.

Hauksson, E, L.M. Jones, K. Hutton, and D. Eberhart-Phillips, The 1992, Landers earthquake sequence: Seismological observations, *J. Geophys. Res.*, *98*, 19,835-19,858, 1993.

Hart, E.W., W.A. Bryant, and J.A. Treiman, Surface faulting associated with the June 1992 Landers earthquake, California, *Calif. Geol.*, *46*, 10-16, 1993.

Hudnut, K.W., et al., Coseismic displacements of the 1992 Landers earthquake sequence, *Bull. Seismol. Soc. Am.*, *84*, 806-816, 1994.

Kanamori, H., and D. Anderson, Amplitude of the Earth's free

oscillations and long period characteristics of the earthquake source, *J. Geophys. Res.*, *80*, 1075-1078, 1975.

Li, V.C., S.H. Seale, and T. Cao, Postseismic stress and pore pressure readjustment and aftershock distributions, *Tectonophysics*, *144*, 37-54, 1987.

Li, Y.G., T.H. Henyey, and P.C. Leary, Seismic reflection constraints on the structure of the crust beneath the San Bernardino Mountains, Transverse Ranges, southern California, *J. Geophys. Res.*, *97*, 8817-8830, 1992.

Li, Y.G., W.L. Ellsworth, C.H. Thurber, P.E. Malin, and K. Aki, Fault zone guided waves from explosions in the San Andreas Fault at Parkfield and Cienega Valley, California, *Bull. Seismol. Soc. Am.*, *87*, 210-221, 1997.

Linde, A.T., K. Suyehiro, S. Miura, I.S. Sacks, and A. Takagi, Episodic aseismic earthquake precursors, *Nature*, *334*, 513-515, 1988.

Lockner, D.A., and J.D. Byerlee, Dilatancy in hydraulically isolated fautls and the suppression of instability, *Geophys. Res. Lett.*, *21*, 2353-2356, 1994.

MacKenzie, J.K., The elastic constants of a solid containing spherical holes, *Proc. Phys. Soc. London B*, *63*, 1-11, 1950.

Massonnet, D., and K. Feigl, Discrimination of geophysical phenomena in satellite radar interferograms, *Geophys. Res. Lett.*, *22*, 1537-1540, 1995.

Massonnet, D., M. Rossi, C. Carmona, F. Adragna, G. Peltzer, K. Feigl, and T. Rabaute, The displacement field of the Landers earthquake mapped by radar interferometry, *Nature*, *364*, 138-142, 1993.

Massonnet, D., W. Thatcher, and H. Vadon, Detection of postseismic fault-zone collapse following the Landers earthquake, *Nature*, *382*, 612-616, 1996.

Michelini, A., and T.V. McEvilly, Seismological studies at Parkfield, I., Simultaneous inversion for velocity structure and hypocenters using cubic B-splines parametrisation, *Bull. Seismol. Soc. Am.*, *81*, 524-552, 1991.

Muir-Wood, R., and G.C.P. King, Hydrological signatures of earthquake strain, *J. Geophys. Res.*, *98*, 22,035-22,068, 1993.

Murakami, M., M. Tobita, S. Fujiwara, T. Saito, and H. Masaharu, Coseismic crustal deformations of 1994 Northridge, California, earthquake detected by interferometric JERS1 synthetic aperture radar, *J. Geophys. Res.*, *101*, 8605-8614, 1996.

Nur, A., and J. R. Booker, Aftershocks caused by pore fluid flow?, *Science*, *175*, 885-887, 1972.

Okada, Y., Surface deformation due to shear and tensile faults in a half-space, *Bull. Seismol. Soc. Am.*, *75*, 1135-1154, 1985.

Peltzer, G., and P. Rosen, Surface displacement of the 17 May 1993 Eureka Valley, California, earthquake observed by SAR interferometry, *Science*, *268*, 1333-1336, 1995.

Peltzer, G., K. W. Hudnut, and K. Feigl, Analysis of coseismic surface displacement gradients using radar interferometry: New insights into the Landers earthquake, *J. Geophys. Res.*, *99*, 21,971-21,981, 1994.

Peltzer, G., P. Rosen, F. Rogez, and K. Hudnut, Fault creep and slow deformation processes detected with SAR interferometry, *Eos Trans. AGU*, *77*(46), Fall Meet. Suppl., F49, 1996a.

Peltzer, G., P. Rosen, F. Rogez, and K. Hudnut, Postseismic rebound in fault step overs caused by pore fluid flow, *Science*, *273*, 1202-1204, 1996b.

Pollitz, F.F., Gravitational viscoealstic postseismic relaxation on a layered spherical Earth, *J. Geophys. Res.*, *102*, 17,921-17,941, 1997.

Rice, J.R., and M.P. Cleary, Some basic stress diffusion solutions for fluid-saturated elastic porous media with compressible constituents, *Rev. Geophys.*, *14*, 227-241, 1976.

Roeloffs, E., Poroelastic techniques in the study of earthquakes-related hydrologic phenomena, *Adv. Geophys.*, *37*, 135-195, 1996.

Rosen, P., S. Hensley, Y. Lou, S. Shaffer, and E. Fielding, A digital elevation model from Oregon to Mexico derived from SIR-C radar interferometry, *Eos Trans. AGU*, *76*(46), Fall Meet. Suppl., F64, 1995.

Rudnicki, J.W., and C.H. Chen, Stabilization of rapid frictional slip on a weakening fault by dilatant hardening, *J. Geophys. Res.*, *93*, 4745-4757, 1988.

Sato, Y., Velocity of elastic waves propagated in media with small holes, *Bull. Earthquake Res. Inst. Univ. Tokyo*, *30*, 178-190, 1952.

Sauber, J., W. Thatcher, S.C. Solomon, and M. Lisowski, Geodetic slip rate for the Eastern California Shear Zone and the recurrence time of Mojave Desert earthquakes, *Nature*, *367*, 264-266, 1994.

Savage, J.C., and J.L. Svarc, Postseismic deformation associated with the 1992 M_w=7.3 Landers earthqake, southern California, *J. Geophys. Res.*, *102*, 7565-7577, 1997.

Savage, J.C., M. Lisowski, and W.H. Prescott, An apparent shear zone trending north-northwest across the Mojave Desert into Owens Valley, eastern California, *Geophys. Res. Lett.*, *17*, 2113-2116, 1990.

Shen, Z.K., D. Jackson, Y. Feng, M. Cline, M. Kim, P. Fang, and Y. Bock, Postseismic deformation following the Landers earthquake, California, 28 June 1992, *Bull. Seismol. Soc. Am.*, *84*, 780-791, 1994.

Shifflett, H., and R. Whitbaard, Premonitory precursors to the Landers earthquake, *Eos Trans. AGU*, *76*(46), Fall Meet. Suppl., F359-F360, 1995.

Sieh, K., et al., Near-field investigations of the Landers earthquake sequence, April to July 1992, *Science*, *260*, 171-176, 1993.

Sleep, N.H., and M.L. Blanpied, Creep, compaction and the weak rheology of major faults, *Nature*, *359*, 687-692, 1992.

Sleep, N.H., and M.L. Blanpied, Ductile creep and compaction: A mechanism for transiently increasing fluid pressure in mostly sealed fault zones, *Pure Appl. Geophys.*, *143*, 1-40, 1994.

Sowers, J.M., J.R. Unruh, W.R. Lettis, and T.D. Rubin, Relationship of the Kickapoo fault to the Johnson Valley and Homestead Valley faults, San Bernardino County, California, *Bull. Seismol. Soc. Am.*, *84*, 528-536, 1994.

Spotila, J. A., and K. Sieh, Geologic investigation of a "slip gap" in the surficial ruptures of the 1992 Landers earthquake, southern California, *J. Geophys. Res.*, *100*, 545-559, 1995.

Sylvester, A., Investigation of nearfield postseismic slip following the M_w 7.3 Landers earthquake sequence of 28 June 1992, California, *Geophys. Res. Lett.*, *20*, 1079-1082, 1993.

Thurber C., Creep events preceeding small to moderate earthquakes on the San Andreas fault, *Nature*, *380*, 425-428, 1996.

Wald, D.J., and T.H. Heaton, Spatial and temporal distribution of slip for the 1992, Landers, California earthquake, *Bull. Seismol. Soc. Am.*, *84*, 668-691, 1994.

Wdonwinski, S., Y. Bock, J. Zhang, P. Fang, and J. Genrich, Southern California permanent GPS geodetic array: Spatial filtering of daily position for estimating coseismic and postseismic displacement induced by the 1992 Landers earthquake, *J. Geophys. Res.*, *102*, 18,057-18,070, 1997.

Yu, T.T., J.B. Rundle, and, J. Fernandez, Surface deformation due to a strike-slip fault in an elastic gravitational layer overlying a viscoelastic gravitational half-space, *J. Geophys. Res.*, *101*, 3199-3214, 1996.

Zebker, H.A., C. Werner, P. Rosen, and S. Hensley, Accuracy of topographic maps derived from ERS-1 interferometric radar, *IEEE Trans. Geosci. Remote Sens.*, *32*, 823-836, 1994a.

Zebker, H. A., P. Rosen, R.M. Goldstein, A. Gabriel, and C.L. Werner, On the derivation of coseismic displacement fields using differential radar interferometry: The Landers earthquake, *J. Geophys. Res.*, *99*, 19,617-19,634, 1994b.

Zebker, H.A., P. A. Rosen, and S. Hensley, Athmospheric effects in interferometric synthetic-aperture radar surface deformation and topographic maps, *J. Geophys. Res.*, *102*, 7547-7563, 1997.

G. Peltzer, F. Rogez, and P. Rosen, JPL/MS 300-233, 4800 Oak Grove Drive, Pasadena, CA 91109. (gilles@altyn.jpl.nasa.gov)

K. W. Hudnut, U. S. Geological Survey, 525 South Wilson Avenue, Pasadena, CA 91106-3212.

(Received February 18, 1998; revised June 11, 1998; accepted July 6, 1998.)